Slug Bubbling in Flat Sheet MBRs: Hydrodynamic Optimization of Membrane Design Variables through Computational and Experimental Studies

Bing Wang[a,b], Kaisong Zhang[a,b*], Robert W. Field[c]

[a] *Key Laboratory of Urban Pollutant Conversion, Institute of Urban Environment, Chinese Academy of Sciences, Xiamen 361021, China*

[b] *University of Chinese Academy of Sciences, Beijing 100049, China*

[c] *Department of Engineering Science, University of Oxford, Oxford OX1 3PJ, UK*

* Corresponding author: KS Zhang, kszhang@iue.ac.cn

Paper prepared for Journal of Membrane Science 2017

Abstract

Slug bubbling in flat sheet MBRs (FSMBR) is of interest in water treatment industry to effectively control fouling. In this work, a novel bubbling method is used to produce slug bubbles into all channels between every pair of membranes for a large-scale 100-sheets commercial FSMBR. Below the membrane plates, coalescent bubbles formed and these developed into large-sized bubbles, which eventually distributed between channels as a set of slug bubbles. Computational Fluid Dynamics (CFD) was used to predict the bubble size and distribution among different channels, and associated hydrodynamic features. Substantial agreement was observed with the experiment results. The configuration of membrane plate centrally located above the aeration nozzles was determined to have superior hydrodynamic performance of high shear stress on the membrane surfaces. The effect of membrane plate and channel dimensions were studied to identify the optimized design for hydrodynamics enhancement on fouling control. The combination of membrane thickness at 5mm and channel gap at 6mm was verified to be the optimal configuration, which would give uniform distribution of slug bubbles and provide high shear stress in the channels. The optimized air flow rate was successfully reduced to 4.7 L/min•m^2, which corresponds to a 53% reduction compared with traditional usage (10 L/min•m^2) in industry.

Key Words

Flat sheet MBR; coalescent bubbling; slug bubble; CFD; fouling control.

1. Introduction

The membrane bioreactor (MBR) technology is a reliable technology that is widely used for the treatment and reclamation of both industrial and municipal wastewaters. However, membrane fouling remains the major drawback impeding the wider application of the MBR technology because the consequences are that it results in higher energy costs and membrane replacement expenditure [1-5]. Therefore, various aeration processes have been developed as a technically effective strategy for fouling control and oxygen transfer process [6-11].

The aeration for slug bubbling was early studied by Cui et al., which could enhance the surface shear, effectively control concentration polarization and subsequently ameliorate membrane fouling [1, 6, 8]. The hydrodynamic effect introduced by slug bubbles on flat sheet MBRs (FSMBR) were also investigated in our previous studies. High wall shear stress could be induced by periodic slug bubbles in FSMBR which is more effective and economic to enhance the mass transfer coefficient with a modest consumption of air [3]. Electrochemical experiments and numerical studies on one membrane sheet surface had shown that shear stress from over 60 mL slug bubble could produce excellent spanwise shear stress of more than 1.0 Pa on the flat membrane, thus greatly enhancing fouling mitigation [4]. As noted previously shear stress of >1.5 Pa from slug bubble inside one channel between two membrane plates could be efficient and beneficial for fouling control [12]. The need to generate the slug bubbles with high hydrodynamic performance for a large-scale commercial FSMBR with 100 membrane sheets led to a novel slug bubbling process. A systematic study to generate an optimal design was the subject of this work.

Since the aeration process has significant effect on fouling control and high energy cost, the influence of different MBR design parameters and structures on the two-phase flow were studied. Prieske et al. [13] evaluated the shear stress exerted by the rising bubbles from optimizing

the geometries of tank and module accordingly in order to obtain an improved deposition control at minimum energy input. Liu et al. [14] studied the combination of features for the hollow fiber membrane module, filtration tank, and aeration system to achieve larger homogeneous shear in the filtration zone. Similarly, Taha et al. [8] related the slug bubbling frequency, bubble size with permeate flux in the tubular membrane system, and found that the wall shear rate and flux were highest when the membrane was inclined at 45° from the horizontal position. Drews et al. [15] investigated the wall shear that a single bubble induced could be dependent on the membrane plate spacing (3-9 mm) and bubble size (3-10mm), the air sparging could have advantageous but also detrimental effects on the wall shear. Yamanoi and Kageyama [16] also reported that the large bubbles (11–21mm) with two-dimensional amorphous shapes between membranes could result in a larger shear stress compared to the bubbles (3.7-10mm) which was smaller than the membrane clearance in an FSMBR. Culfaz et al. [17] found that large, cap-shaped bubbles and slugs had better performance than small bubbles in Hollow Fiber MBRs.

However, large amount of fundamental research has focused on tubular and hollow fiber membrane modules [18-20]. Although growing, the literature on aeration optimization and slug bubbling in FS format was still quite limited [16, 21]. Furthermore, the method to produce slug bubbles for a commercial large-scale FSMBR (i.e., 100 membrane sheets) was still needed. This in turn necessitated more fundamental research on the hydrodynamics of slug bubbling with different design variables in a large-scale FSMBR, which could effectively control the fouling at an economical energy consumption. The aim of the present work is to optimize the configuration of aerator and membrane plates for a novel aeration process of slug bubbles in a large-scale commercial FSMBR wherein one can modify and efficiently control the wall shear stress to enhance the hydrodynamic effect whilst reducing the energy demand. Computational Fluid

Dynamics (CFD) simulation and experiment approaches were both utilized to precisely predict bubble generation process and coalescent features. Particular emphasis was given to the bubble distribution into channels between every pair of membranes. The wall shear stress was compared and analyzed in each channel at different configurations to achieve more uniform distribution, and higher values of wall shear stress as well as an economical air flow rate.

2. Methods

2.1 Experiment Method

The bubbles were generated from an aerator of O.D.20mm with 4 nozzles (Fig. 1). The aerator was fixed in the bottom of a large-scale plexiglass tank with the dimensions of 510×600×1800 mm (Length×Thickness×Height). Deionized water was filled in the tank as the liquid phase, then 15 membrane plates (provided by Oxiamembrane Co., Ltd, Xiamen, China) with the dimensions of 510×5×1200 mm (Length×Thickness×Height) was placed above the aerator. The distance of the membranes to aerator was 360 mm. One of the channels was formed by a sheet of transparent plexiglass with the same dimensions and a membrane to unobtrusively observe the bubble development inside the channel.

Compressed air was directed by air pump to the liquid tank under air flow rate of 36.2 L/min. Solenoid valve with a time controller was used to generate intermittent aeration at a fixed open time of 1Hz. Buffer tank was connected between the solenoid valve and air rotameter to dampen the upstream air flow pulsation. The slug bubbling process was observed and recorded by a high-speed CMOS camera (FASTCAM-ultima APX, Photron, Japan) with 1024×1024-pixel resolution. The images were processed by MATLAB program to obtain the quantitative features

of the large size bubble formation process during its upwards movement. All experiments were repeated three times and conducted at room temperature.

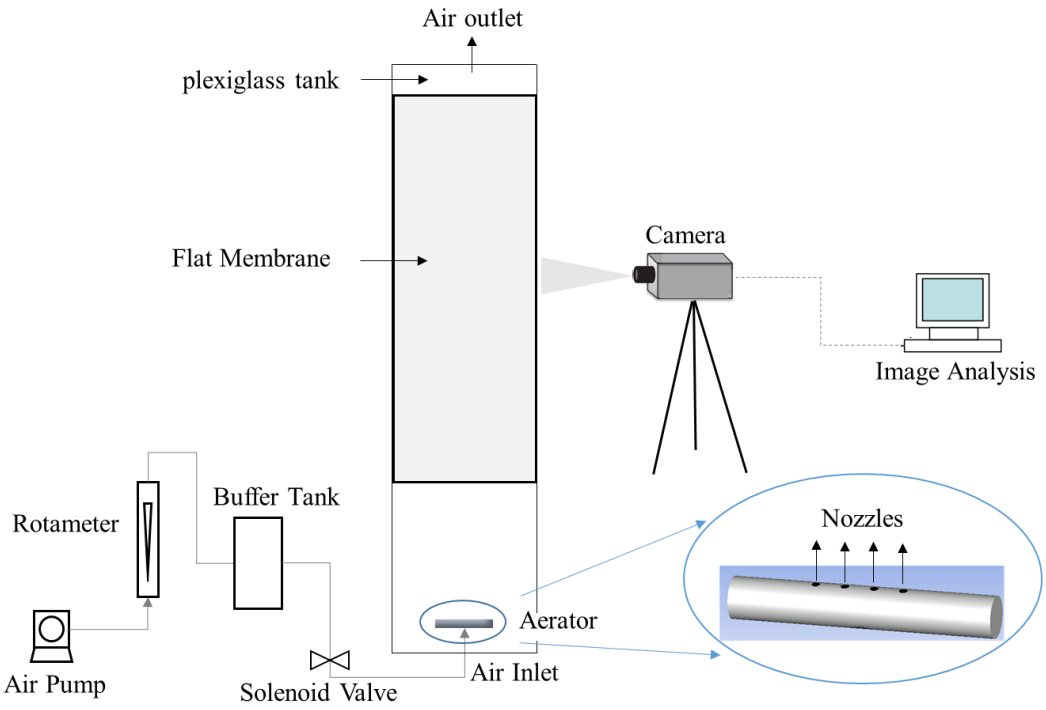

Fig. 1 Schematic diagram of slug bubbling experimental rig.

2.2 Numerical Simulation Method

2.2.1 Physical model and meshing

Hydrodynamic characteristic of the novel bubbling process was studied by Computational Fluid Dynamics (CFD) simulations. 3D numerical modeling was conducted for two configurations of different aerator positions, in which the aerator was placed below the membrane (Fig. 2 (a)) and below the channel (Fig. 2 (b)), respectively.

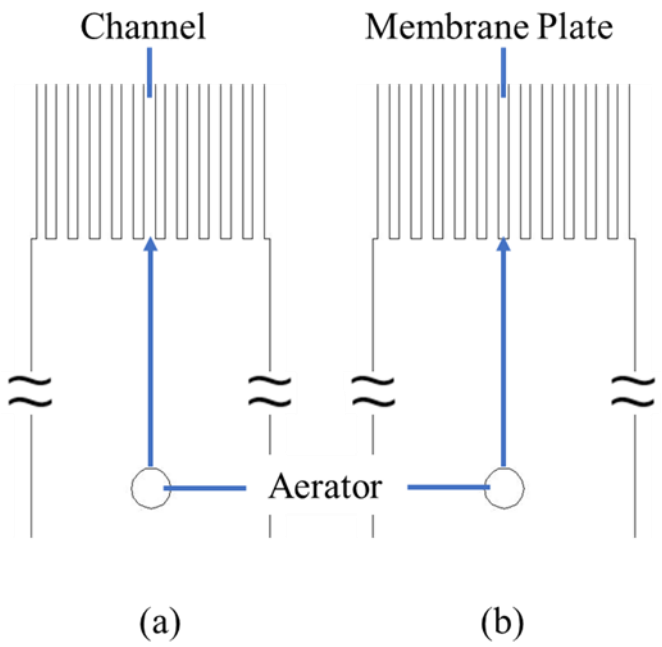

Fig. 2 Two types of configurations of aerator (side view): (a) Configuration 1: nozzles below the central channel; (b) Configuration 2: nozzles below the center of the middle membrane plate.

Moreover, the thickness of membrane plates and channels were adjusted and detail information of geometries used in simulations was collected in Table 1. Various computational domains were set up according to different geometries by using GAMBIT 2.4.6 software and the mesh information was shown in Table 1. The Cooper-type hex mesh was constructed for the computational domain with symmetric boundary conditions which could save computational time by a factor of 4. One of the computation domain was shown in Fig. 3, which contained 2,356,256 cells, 7,627,720 faces and 2,915,960 nodes. No individual cell had a value of larger than 0.69 for EquiSize Skew parameter. This high-quality mesh could directly impact simulation time and convergence stability. Moreover, for all the computational domains, the value of average EquiSize

Skew parameters were all within the range from 0.2 to 0.3 (0-best; 1-worst), suggesting that the mesh quality of the computational model is excellent.

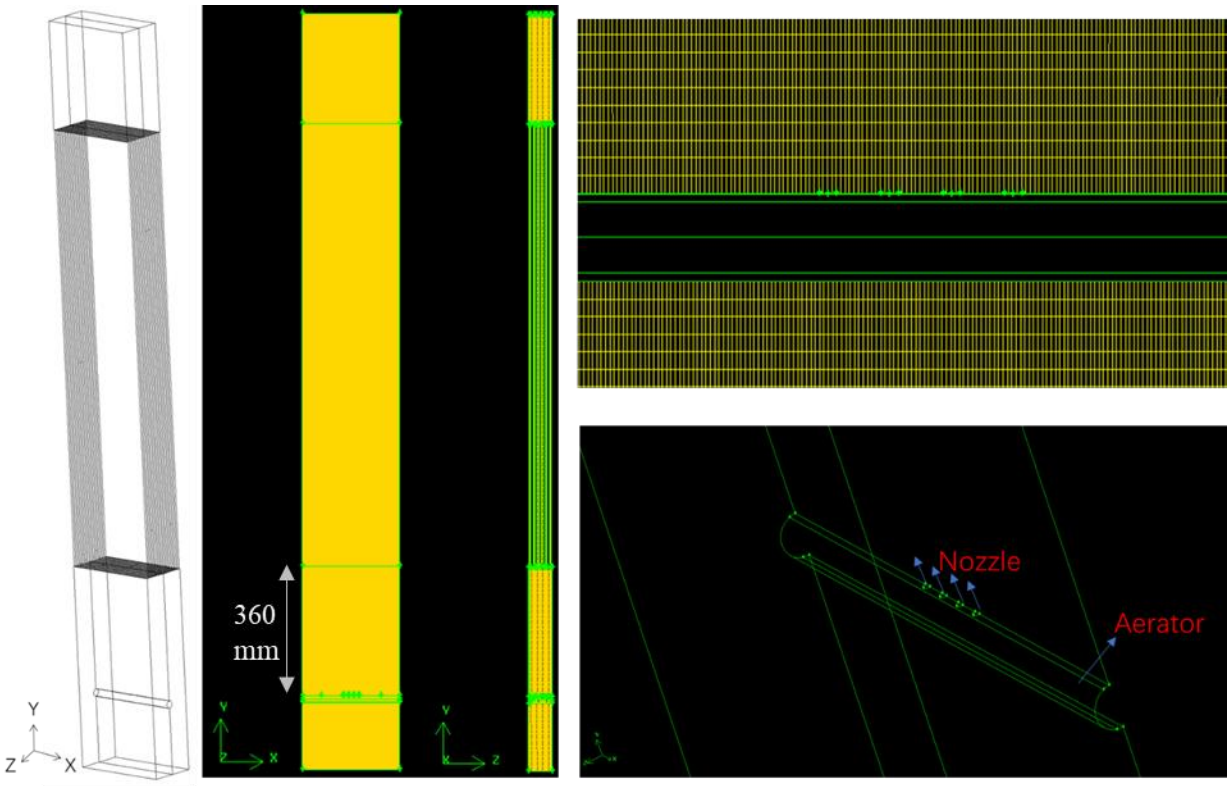

Fig. 3 Mesh structure of computational domain generated by GAMBIT software: membrane plate thickness of 5mm and channel gap of 6mm.

Table 1 Mesh information for various 3D computational geometries

Aerator below the channel

Name	Width of Membrane Plate (mm)	Width of Channel (mm)	Number of Cells	Number of Faces	Number of Nodes
--	5	6	2,602,561	8,350,908	3,148,100

Aerator below the membrane plate

Name	Width of Membrane Plate (mm)	Width of Channel (mm)	Number of Cells	Number of Faces	Number of Nodes
M5C4	5	4	2,003,227	6,477,701	2,472,537
M5C5	5	5	1,852,563	6,027,075	2,322,971
M5C6	5	6	2,356,256	7,627,720	2,915,960
M5C6.5	5	6.5	2,255,019	7,333,557	2,823,998
M5C7	5	7	2,392,525	7,744,386	2,960,063
M5C8	5	8	2,529,909	8,003,205	2,994,110
M3C6	3	6	3,148,265	10,027,727	3,732,956
M4C6	4	6	2,356,256	7,627,720	2,915,960
M6C6	6	6	2,255,019	7,333,557	2,823,998

M7C6	7	6	2,211,707	7,719,466	2,747,483
M8C6	8	6	2,192,095	7,043,651	2,661,083

2.2.2 Governing equations

3D simulations were conducted by ANSYS FLUENT 17.0. Among several multi-phase models, VOF (Volume of Fluid) model was used to compute the motion of large bubbles in liquid through incorporating an additional volume fraction equation [22]. The simulation was implemented by solving mass and momentum conservation equations, and additional equations for turbulence and interface tracking. The mass and momentum conservation equations can be expressed as

$$\frac{\partial \rho}{\partial t} + \nabla(\rho \vec{u}) = 0 \quad (1)$$

$$\frac{\partial}{\partial t}(\rho \vec{u}) + \nabla(\rho \vec{u}\vec{u}) = -\nabla P + \rho \vec{g} + \rho \vec{F} + \nabla \vec{\tau} \quad (2)$$

where P, $\vec{g}$ and $\vec{F}$ were the pressure, gravitational acceleration, and external force, respectively. The properties appearing in the transport equations were determined by the presence of the component phases in each control volume. The volume-fraction-averaged density ρ and dynamic viscosity μ for an n-phase system were defined as

$$\rho = \sum \alpha_q \rho_q \quad (3)$$

$$\mu = \sum \alpha_q \mu_q \quad (4)$$

The volume fraction function was solved using the geometric reconstruction scheme based on piecewise linear interface calculation (PLIC). The primary phase volume fraction of the n-phase system was computed based via the following Eq. (5).

$$\sum_{q=1}^{n} \alpha_q = 1 \quad (5)$$

Turbulence effect induced by the bubbling process was simulated through realizable k–ε model [23]. In this model, k is the turbulence kinetic energy and ε was the dissipation rate. Therefore, two additional transport equations for *k* and *ε* should be solved, shown here as Eqs. (6) and (7), respectively:

$$\frac{\partial}{\partial t}(\rho k)+\frac{\partial}{\partial x_j}(\rho k u_j)=\frac{\partial}{\partial x_j}\left[\left(\mu+\frac{\mu_t}{\sigma_k}\right)\frac{\partial k}{\partial x_j}\right]+G_k+G_b-\rho\varepsilon-Y_M \tag{6}$$

$$\frac{\partial}{\partial t}(\rho\varepsilon)+\frac{\partial}{\partial x_j}(\rho\varepsilon u_j)=\frac{\partial}{\partial x_j}\left[\left(\mu+\frac{\mu_t}{\sigma_\varepsilon}\right)\frac{\partial \varepsilon}{\partial x_j}\right]+\rho C_1 S\varepsilon-\rho C_2\frac{\varepsilon^2}{k+\sqrt{\upsilon\varepsilon}}+C_{1\varepsilon}\frac{\varepsilon}{k}C_{3\varepsilon}G_b+S_\epsilon \tag{7}$$

Where

$$\mu_t=\rho C_\mu\frac{k^2}{\varepsilon}$$

$$C_1=\max[0.43,\frac{\eta}{\eta+5}]$$

$$\eta=S\frac{k}{\varepsilon}$$

$$S=\sqrt{2S_{ij}S_{ij}}$$

In these equations, G_k represented the generation of turbulence kinetic energy due to the mean velocity gradients, G_b was the generation of turbulence kinetic energy due to buoyancy. C_μ was a function of the mean strain, rotation and turbulence fields. Y_M represented the contribution of the fluctuating dilatation in compressible turbulence to the overall dissipation rate. σ_k and σ_ε were the turbulent Prandtl numbers for *k* and *ε*, respectively. S_k and S_ε were user-defined source terms. C_2, $C_{1\varepsilon}$ and $C_{3\varepsilon}$were constants [24, 25].

Surface tension effects along the interface were calculated via the continuum surface force (CSF) model [26]. The surface tension of two phases can be expressed in terms of the pressure jump across the surface as following:

$$p_L - p_G = \sigma k \tag{8}$$

$$\vec{F}_{vol} = \sigma \frac{2\rho\kappa\nabla_{\alpha_G}}{(\rho_L + \rho_G)} \tag{9}$$

Where κ was the surface curvature defined in terms of the divergence of the unit normal, $\hat{n}$:

$$\kappa = \nabla\hat{n}$$

$$\hat{n} = \frac{n}{|n|}, n = \nabla\alpha_q$$

2.2.3 Numerical methods and boundary conditions

The simulations were carried out on a pressure-based solver using commercial software ANSYS FLUENT 17.0. A second order upwind scheme was chosen for momentum, *k*-ε equations discretization. PISO (pressure implicit splitting of operators) was adopted for pressure–velocity coupling. PRESTO! (pressure staggering option) scheme was used for the pressure term discretization. According to the air flow rate in experiment, air velocity at nozzles was calculated to be 12m/s, and liquid velocity from the nozzles was set to zero. Outflow condition was chosen at air outlet of the tank (Fig. 1). The boundaries for the other walls were all stationary and there was a no fluid-slip condition at the membrane surface. The maximum simulation time for the process was set to be 3.0 s.

3. Results and Discussion

3.1 Bubbling Process and Model Validation

At the heart of the conceptual framework of this novel bubbling approach is large-sized bubble production and their subsequent distribution into different channels. The first fundamental step is the formation of a large coalescent bubble in which side-by-side bubbles coalesce simultaneously after coming out from adjacent nozzles. This is shown in Fig. 4 by both experimental images and the corresponding CFD predictions, in which the coalescent bubble rises rapidly upwards and develops into a large-sized bubble. A quantitative comparison plot of bubble size in three dimensions was provided in Fig. 5. These measurements were plotted as the function of the bubble position height (from the bubble to the nozzles). The typical standard deviation of the experiment data was small (<5%), indicating that the results were highly reproducible. Significant agreement can be observed between the experimental and computational results which validated that the CFD modeling approach could give appropriate values of the hydrodynamic features of the bubble.

A preliminary study of grid independence was performed, an increase in the number of nodes was found to have essentially no effect. Also, it was found that the results of simulations based on the mesh shown in this work was in accordance with experimental results. Moreover, Figs. 4-5 indicated this mesh method was somewhat robust approach for simulation.

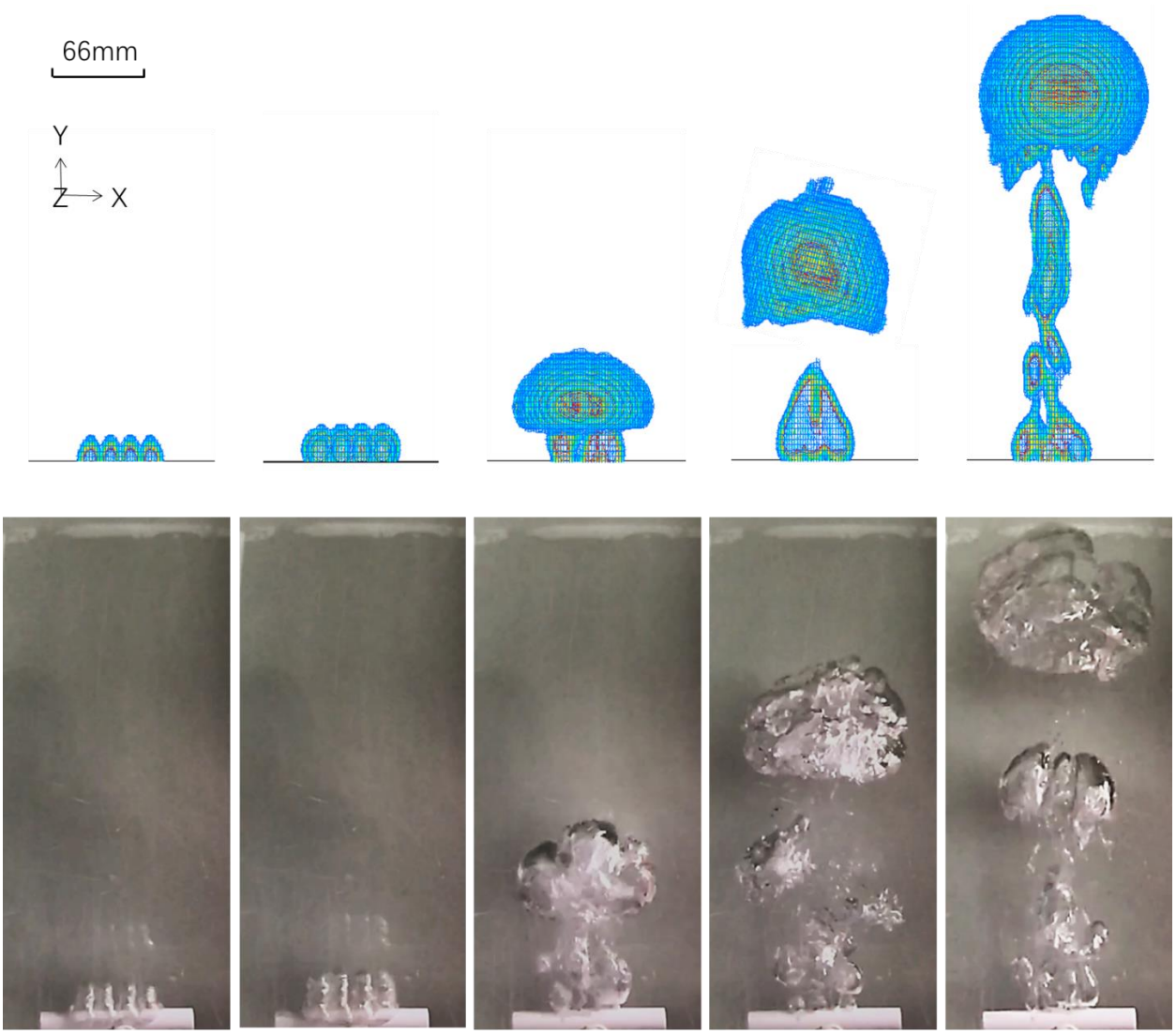

(a)

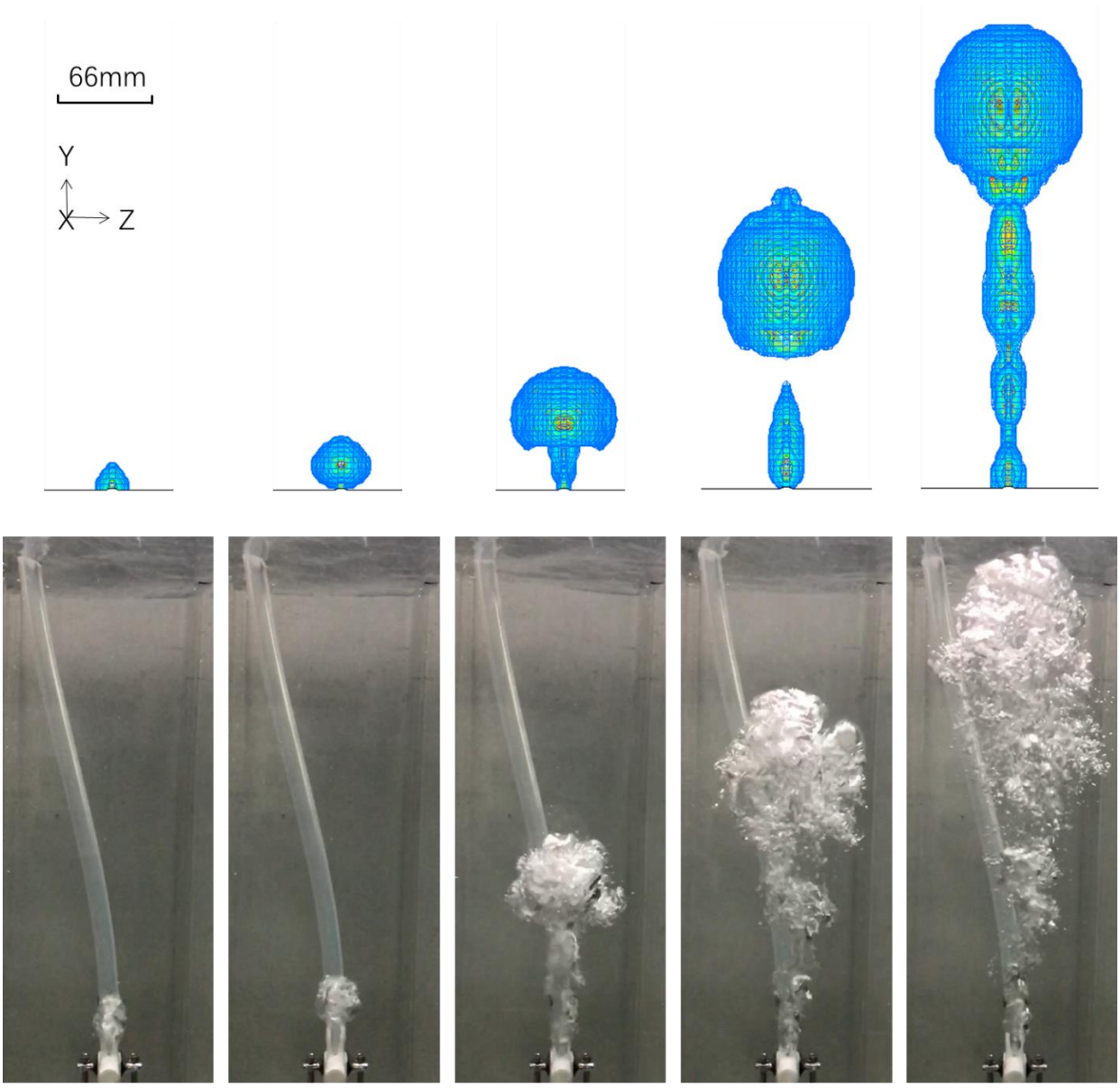

Fig. 4 Bubble coalescence and large-sized bubble development from CFD simulation and experiment results: (a) front view; (b) side view.

As shown in Figs. 4 and 5 of both CFD and experiment results, single bubbles grew in an essentially uniform manner from the different nozzles and rapidly merged together into one

large coalescent bubble. The coalescent bubble continued its growth on the aerator until an imbalance in forces led to its detachment. It should be noted that the bubble sizes in three directions were similar (around 110 mm) when the bubble was at a height of 200mm from the aerator. During its subsequent movement to 350mm height, it remained intact and the bubble size was stable. By 'stable' we referred to the fact that they did not fragment; not to the fact that the shape is invariant.

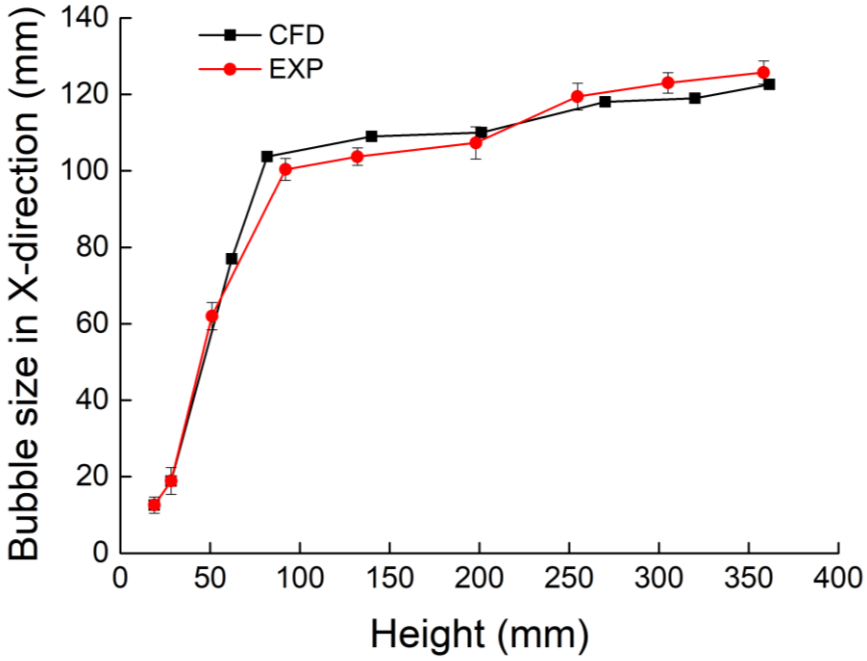

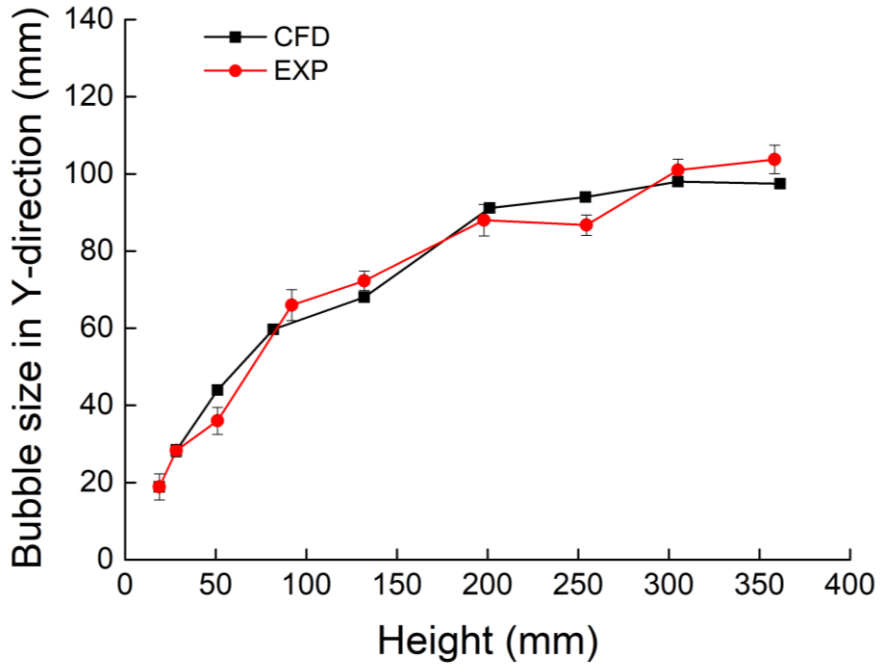

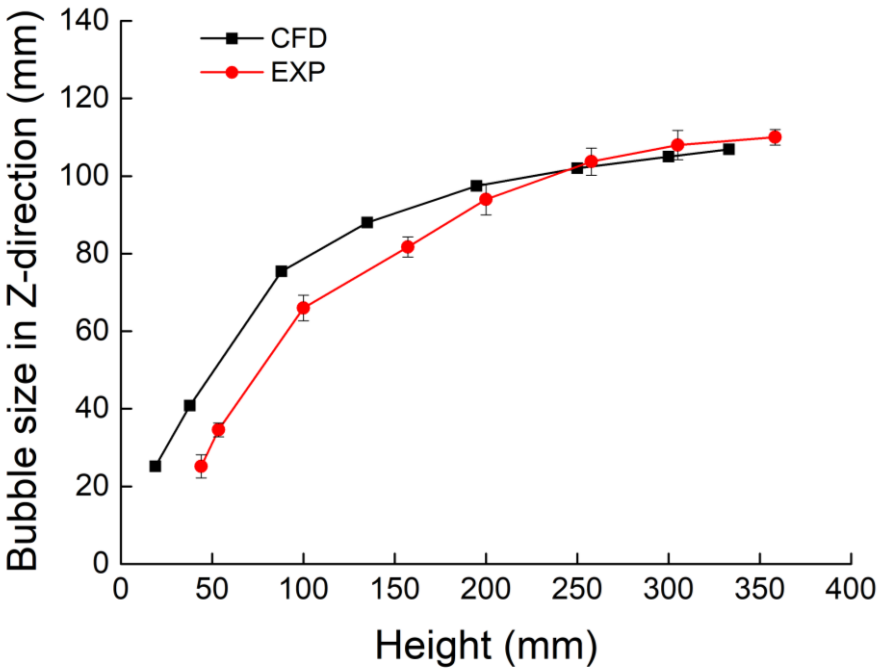

Fig. 5 3 Coalescent bubble size development: a comparison of CFD results with experimental data.

As the stable bubble contacted with the membrane base, it moved upwards rapidly and distributed into channels splitting itself into slug bubbles which rose between every pair of

membranes. This gave slug bubbling between the membranes which could potentially induce an important “hydrodynamic effect” to ameliorate the fouling. These slug bubbles would move upwards through the channels between every pair of membranes as shown in Fig. 6 (a). It indicated that the large-sized bubble split into several bubbles upon the contact with the membrane plates. The CFD simulation results were also compared with experimental images as described in Fig. 6 (b). It was verified by the experimental image which was taken for a channel between a membrane and a sheet of transparent plexiglass. The experimental image showed a slug bubble that has a large spherical cap shape followed by several small bubbles in the wake and this was similar to the CFD simulation.

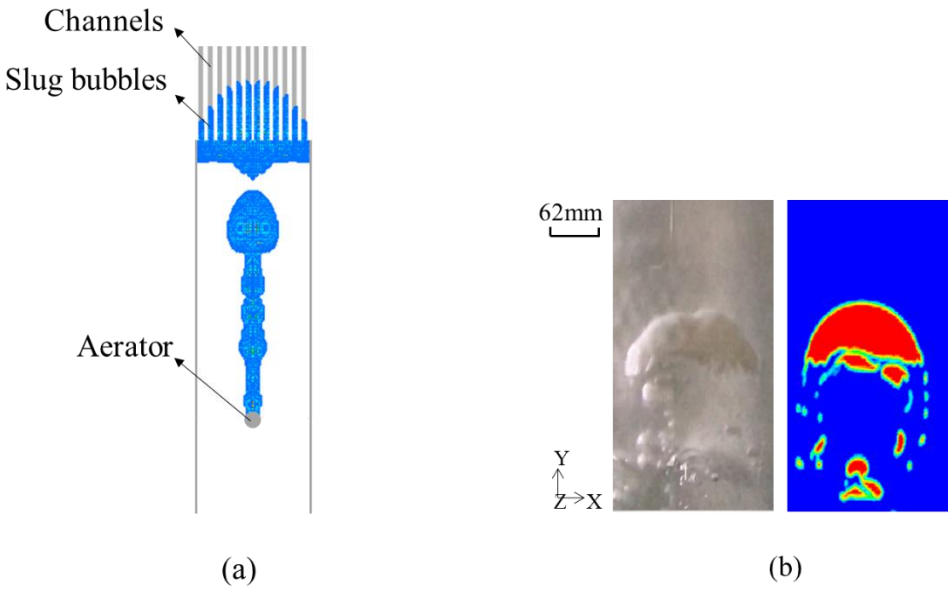

Fig. 6 Views of slug bubble distributed into channels: (a) Side view of CFD results; (b) Front view of experiment image taken between a membrane and a sheet of transparent plexiglass.

Overall it indicated that slug bubbles covering all the channels can be produced from one large-sized coalescent bubble from CFD numerical modeling results which were validated

experimentally. This novel bubbling approach could give potentially beneficial hydrodynamic effects to ameliorate fouling [10]. It could be optimized by the design of aerator, membrane plate and channel configurations.

3.2 Variation of aerator position

This was studied for the two configurations shown in Fig. 2. The CFD predictions for the slug bubbles distribution in 6 channels for two different configurations of aerator is shown in Fig. 7. For configuration 1, the slug bubbles from the aerator broke into two bubbles following by a large numbers of fine bubbles in channel 1, 2, 4 and 6. For configuration 2, in which the nozzle is below the central membrane, slug bubbles of larger size moved through all channels. Bubbles in channel 6 were much smaller with configuration 1 compared to that of configuration 2. This is essentially because the large-sized bubble from the aerator below the central channel distributed more gas into the central channels. For the lateral channels, there was less gas left than that from configuration 2, which indicates less uniformity of bubble distribution with configuration 1. Additionally, excessive gas into one channel made the bubbles unstable causing them to fragment; this is seen in the central region with configuration 1 and it results in a smaller size of slug bubbles. The relatively larger sized slug bubbles in the system with configuration 2 resulted in improved shear stresses as shown in Fig. 8.

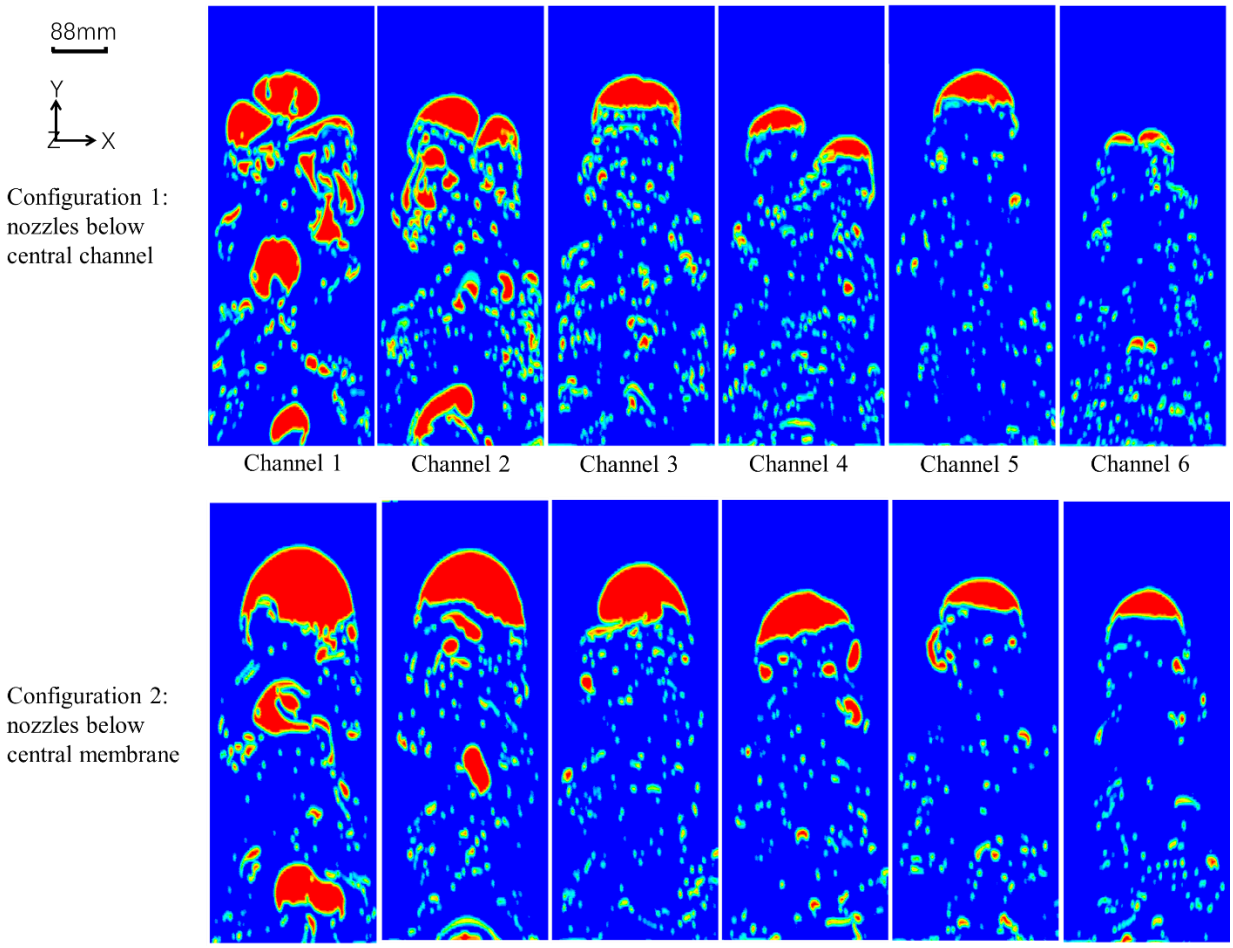

Fig. 7 CFD simulation of bubble distribution in 6 channels from two configurations of aerator.

The shear stress of the split bubbles was characterized as they directly influence the fouling propensity. Wall shear stresses induced by slug bubbles are shown in Fig. 8, in which all of the membrane plates had relatively high shear stress from this novel slug bubbling process. The shear stress values were high and could be more than 5.0 Pa in channel 1 in both cases. For the other channels, some parts of the membrane wall experienced transient shear stresses of between 3-5 Pa with configuration 2. Detailed information is shown in Fig. 8 (b) where the average shear stress was around 3.1 Pa for walls in channel 1-3, and the others were all above 2 Pa from configuration 2. While the stress decreased from 4.4 Pa to 0.6 Pa from channel 1 to channel 6 with

configuration 1, which indicated less effectiveness on fouling control [12], for this configuration. the slug bubbling from configuration 2 could provide higher shear stress to sweep larger area of the membrane surface. The high values of shear stress shown on all membranes, indicates that the system would provide excellent amelioration of fouling and thus high performance [12]. Moreover, in configuration 2 there was a more uniform bubble distribution and consequently a more uniform average shear stress among all channels. This would give more uniform fouling control , an important consideration for industry. Based on the structure of configuration 2, two additional design variables were studied in following sections.

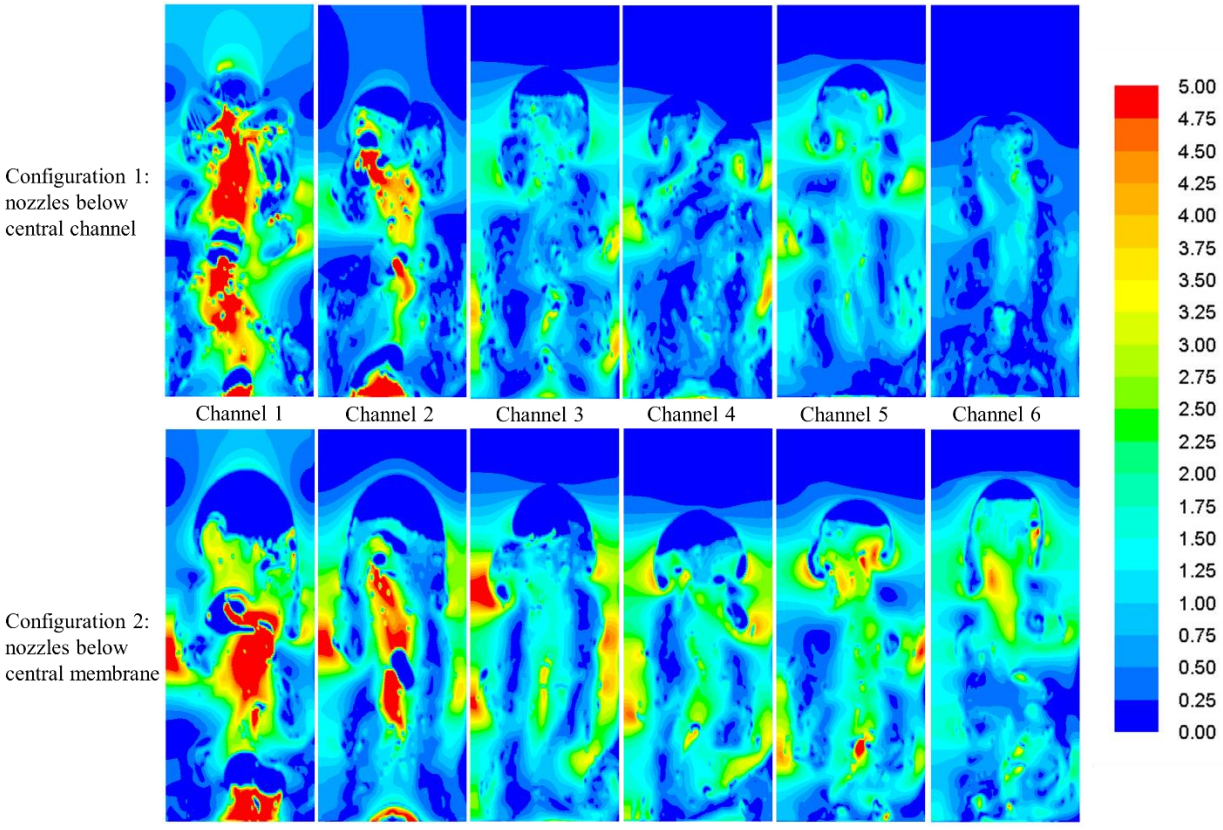

(a)

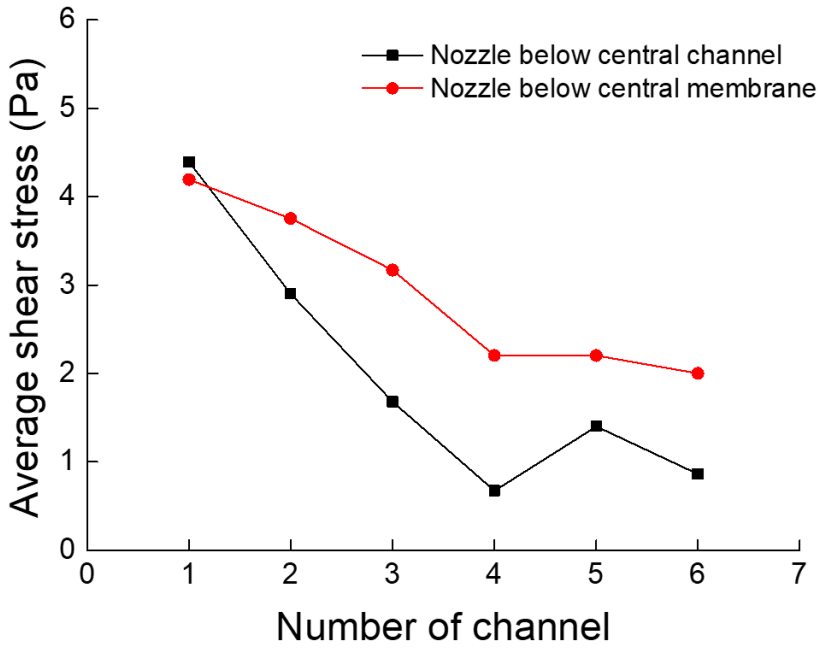

(b)

Fig. 8 (a) Shear stress distribution on membrane walls of each channel. (b) Average shear stress on the wall surfaces in each channel.

3.3 Variation of Channel Gap

For comparative purpose, the slug bubbles were characterized as a function of the channel gap (space between membranes) as shown in Fig. 9. Bubbles that squeezed into channels with a small gap , i.e. 4mm, tend to fragment and form fine bubbles. As the channel gap increased from 4mm to 6mm, the bubble size increased and distribution become uniform among different channels. Especially for the last three channels, the bubbles size was much larger in case M5C6 with gap of 6mm compared to that with M5C4 and M5C5. As the channel gap continued increasing from 6 mm to 8 mm, the bubble distribution uniformity decreased. Bubbles in the last two channels

in the case of M5C8 with its gap of 8 mm were very small and thus ignored. Shear stress for all cases are presented in Fig. 10.

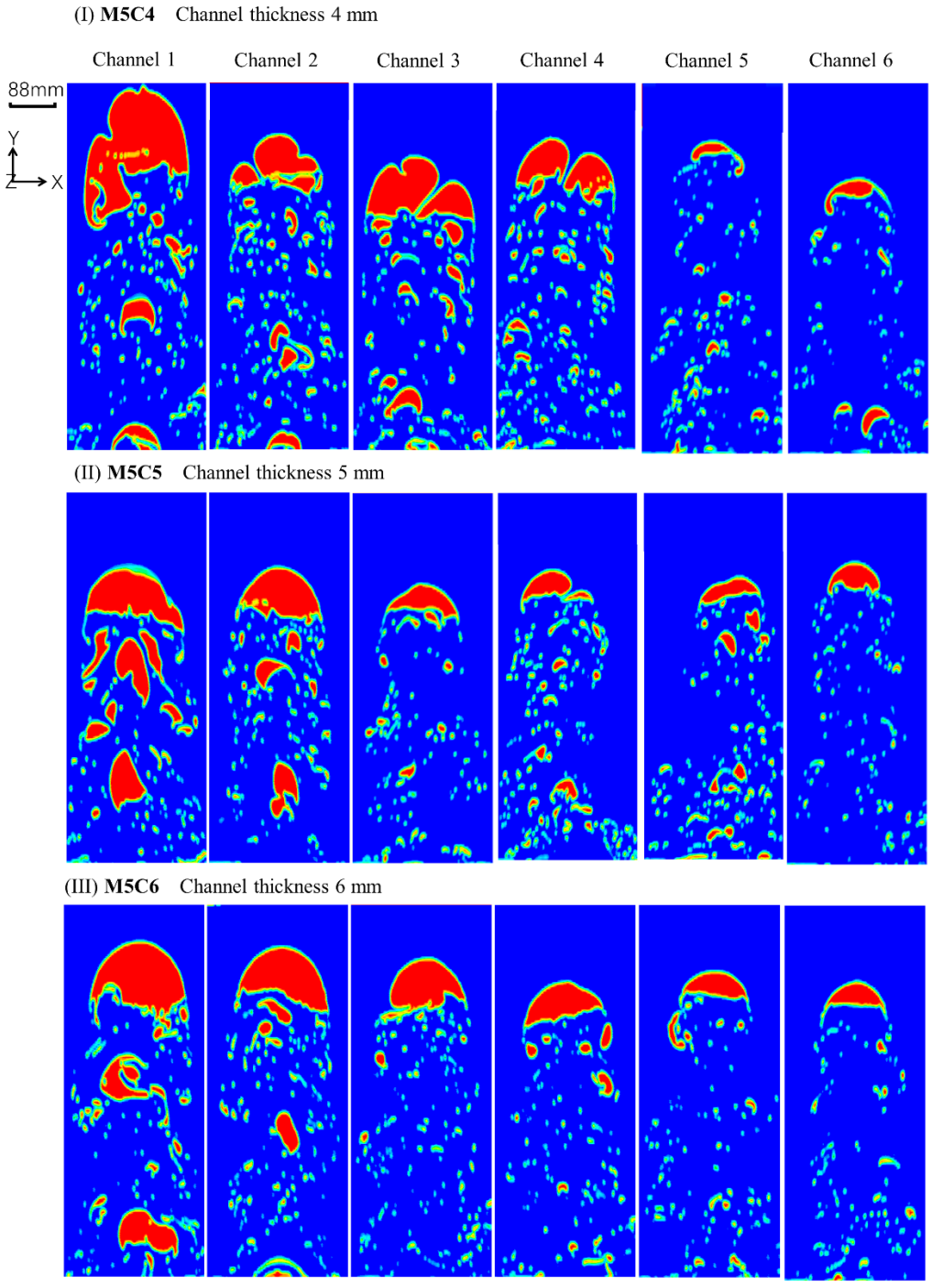

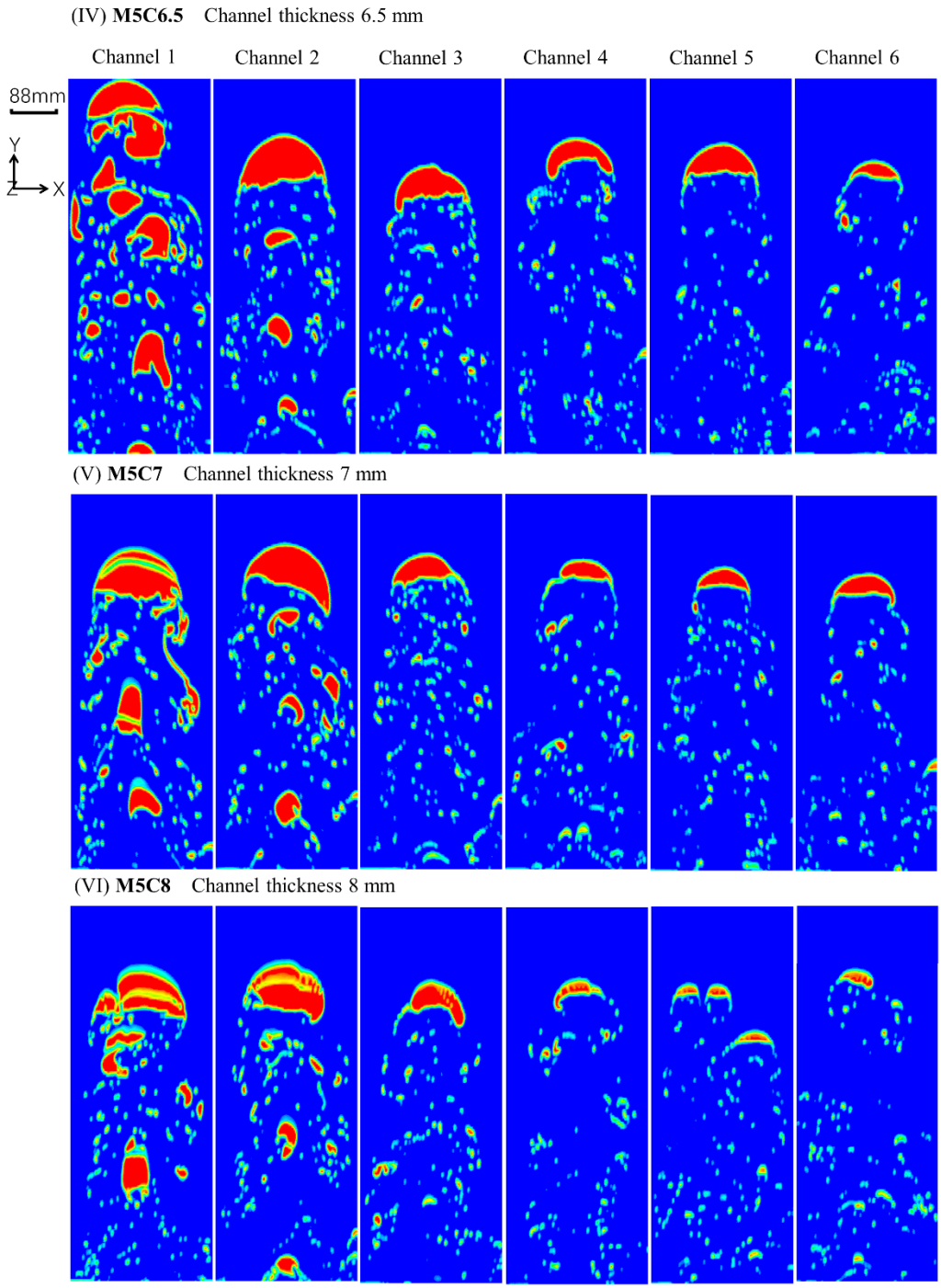

Fig. 9 Bubble distribution comparison for the variation of channel width from 4 mm to 8 mm.

A comparison of the resultant shear stresses was shown in Fig. 10 (a) for 6 channels at different channel gaps. For the first two channels in all cases, shear stress was more than 3.5 Pa

for most parts of the membrane surface, and was more than 5 Pa for the wake regions. For the channels 3 to 6, the shear stress distribution varied as the channel gap increased.

At channel gap of 4mm and 5mm (M5C4 and M5C5), the shear stress of channels 3 to 6 was small and only a few tiny areas were over 2 Pa, and typically around 0.5 Pa for the last two channels. By contrast a higher value of 2.5 Pa and larger areal coverage for channel 3 to 6 was found with M5C6. This gave the optimal hydrodynamic effect. For the condition of M5C6.5 and M5C7, the shear stress was more than 2 Pa for most regions of channel 3 to 6, however it decreased to 1 Pa in some parts of liquid region. While at condition of M5C8, the shear stress was much smaller for the last three channels, which was less than 0.5 Pa for most of regions.

The average shear stress was shown in Fig. 10 (b) for 6 channels at all conditions. The difference of shear stress value between all conditions was less than 1 Pa for the first two channels, which were all over 2.9 Pa. For the other channels from 3 to 6, a larger difference was observed. The maximum difference was more than 1.6 Pa in the last channel. This indicated that the shear stress dramatically decreased away from the central channel to the lateral channel as the channel gap increased. The most uniform shear stress and highest value was found with a channel gap of 6 mm (M5C6), which was also observed in Fig. 10 (a). The shear stress was more than 2 Pa for the 6 channels (1/4 system), which implied an effective performance on fouling control for all the 12 channels (both sides of center) in the entire system from one aerator. . By comparison, in M5C5 and M5C6.5, although shear stress was less than that of M5C6, the novel bubbling approach still yielded good spatial distribution of values in excess of 1.5 Pa, which indicated it could also provide effective fouling control for all 12 channels. As for M5C4, M5C7 and M5C8, the shear stress was less than 1.5 Pa for some channels. Therefore, the channel gap in the range of 5 mm to 6.5 mm

would be a better choice to have higher hydrodynamic effect and uniform shear stress for 12 channels.

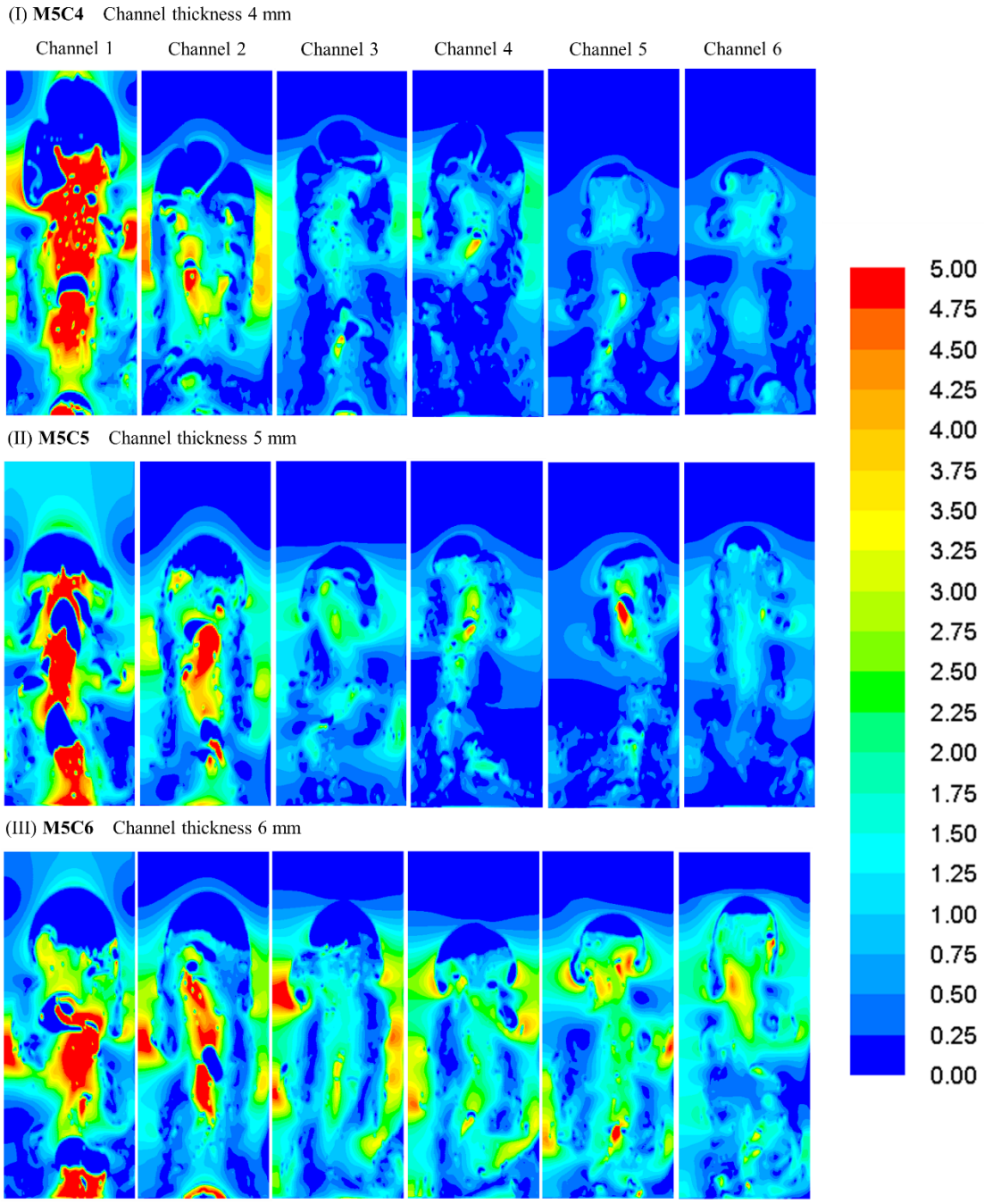

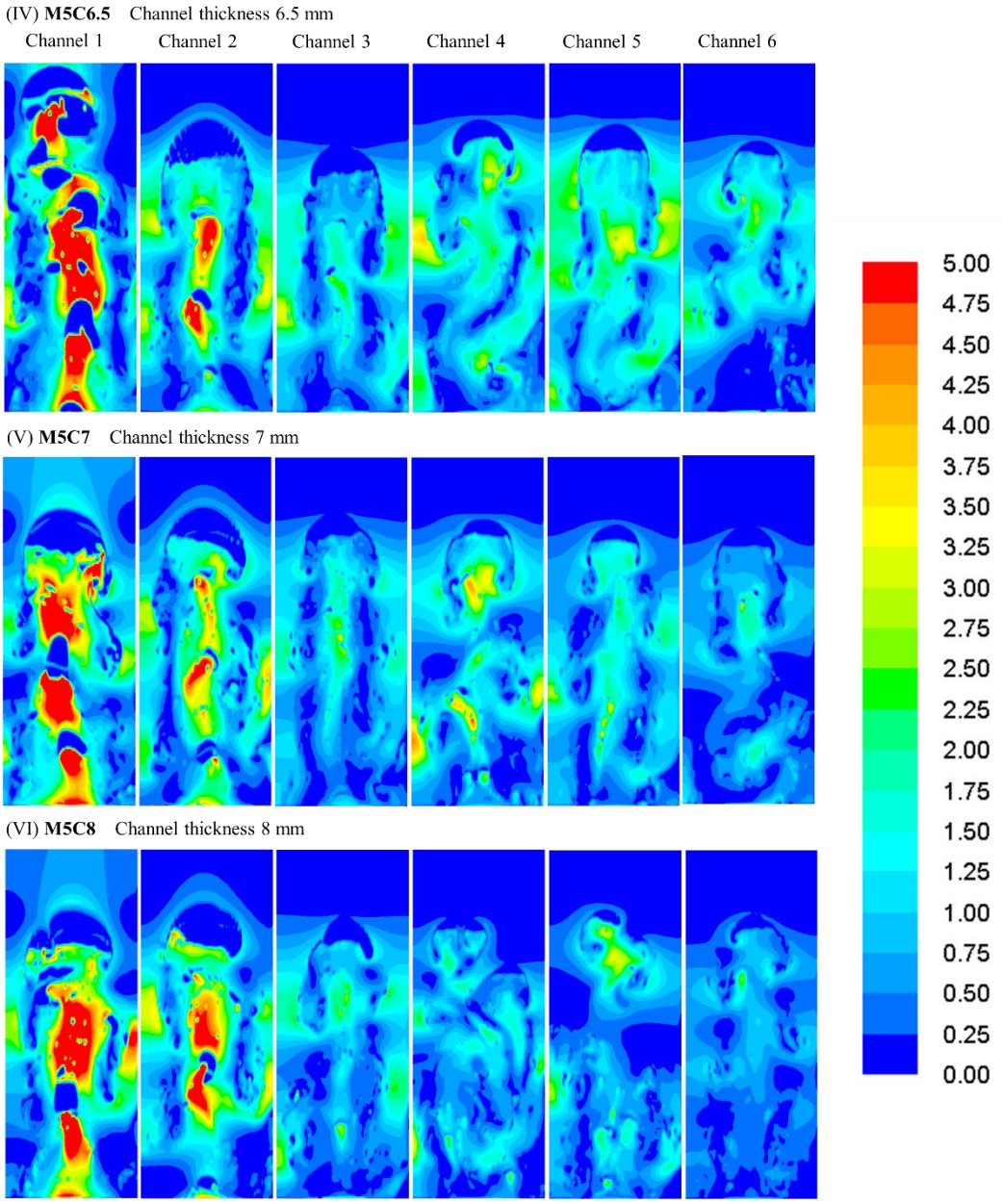
(IV) M5C6.5 Channel thickness 6.5 mm
Channel 1
Channel 2
Channel 3
Channel 4
Channel 5
Channel 6
(V) M5C7 Channel thickness 7 mm
(VI) M5C8 Channel thickness 8 mm
5.00
4.75
4.50
4.25
4.00
3.75
3.50
3.25
3.00
2.75
2.50
2.25
2.00
1.75
1.50
1.25
1.00
0.75
0.50
0.25
0.00

(a)

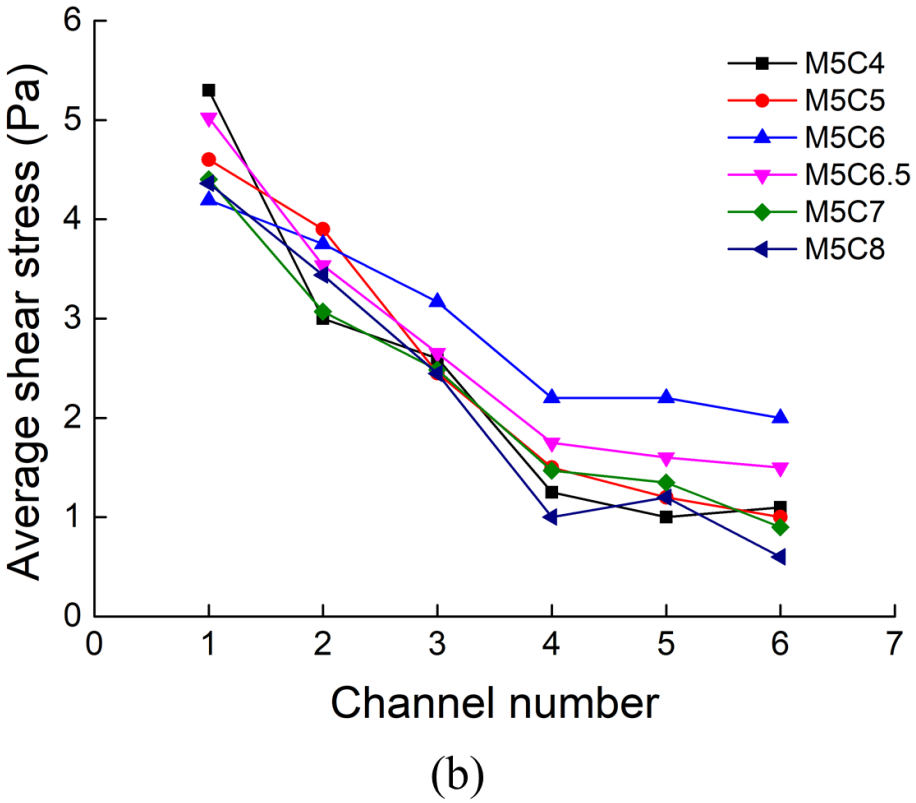

(b)

Fig. 10 Shear stress comparison at different channel gap from 4 mm to 8 mm: (a) shear stress distribution (b) average wall shear stress.

3.4 Variation of Membrane Plate Thickness

For industry, membrane plate thickness is also an important variable in FSMBR design. And therefore its influence was evaluated. found. Different membrane plate thicknesses from 3mm to 8mm were evaluated for the same fixed conditions of 12m/s nozzle velocity and 6mm channel gap. Slug bubbles produced at different membrane plate thicknesses are shown in Fig. 11, which also illustrates the bubble distribution in each channel. For the small thickness of 3mm and 4mm, bubbles in first three channels were of a large size which could cover almost 68% area in the X-direction; while in the last three channels, the bubble size decreased and became almost insignificant in the last two channels. For small thicknesses the results for configuration 2 were

close to those for configuration 1 in Fig. 7. Indeed the bubble distribution in the last few channels were inferior to those in configuration 1.

In Fig. 11, it is seen that the slug bubbles were more uniformly distributed among different channels with the membrane plate thickness of 5mm (M5C6). As the thickness increased to 6mm and 7mm, the distribution uniformity was slightly weakened. However, for the case of 8mm thickness, the bubbles distributed into last few channels were much smaller and bubble tend to fragment resulting in an increased number of fine bubbles. The shear stress induced by bubbles is plotted in Fig. 12.

(I) M3C6 Membrane plate thickness 3 mm

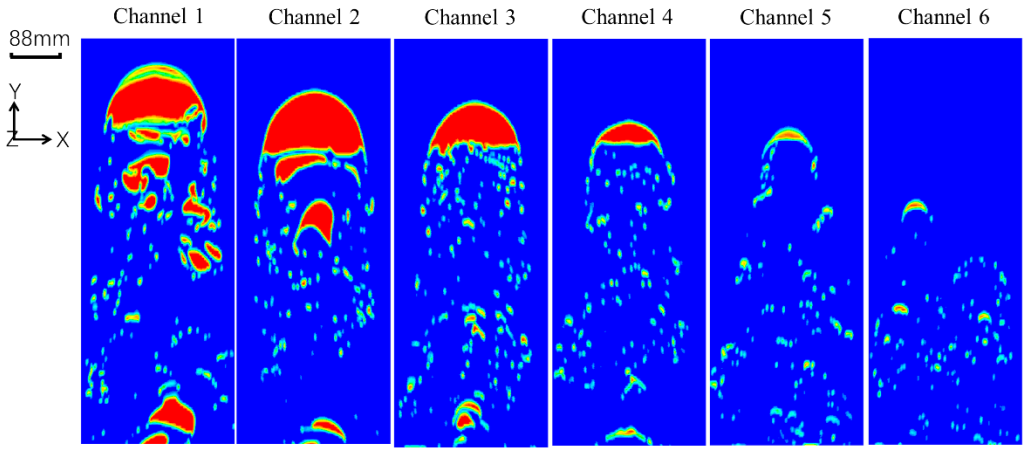

(II) M4C6 Membrane plate thickness 4 mm

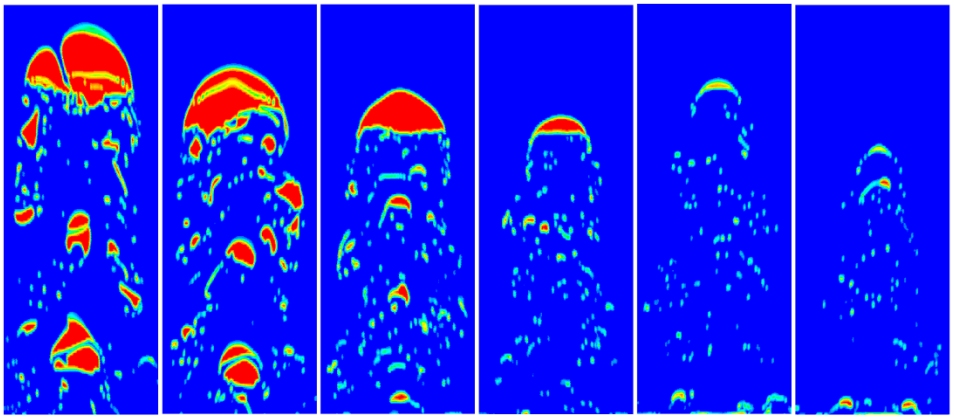

(III) M5C6 Membrane plate thickness 5 mm

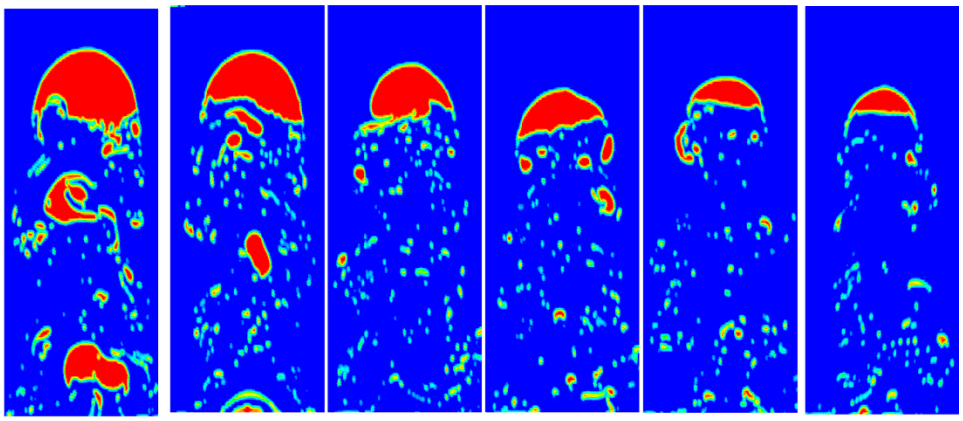

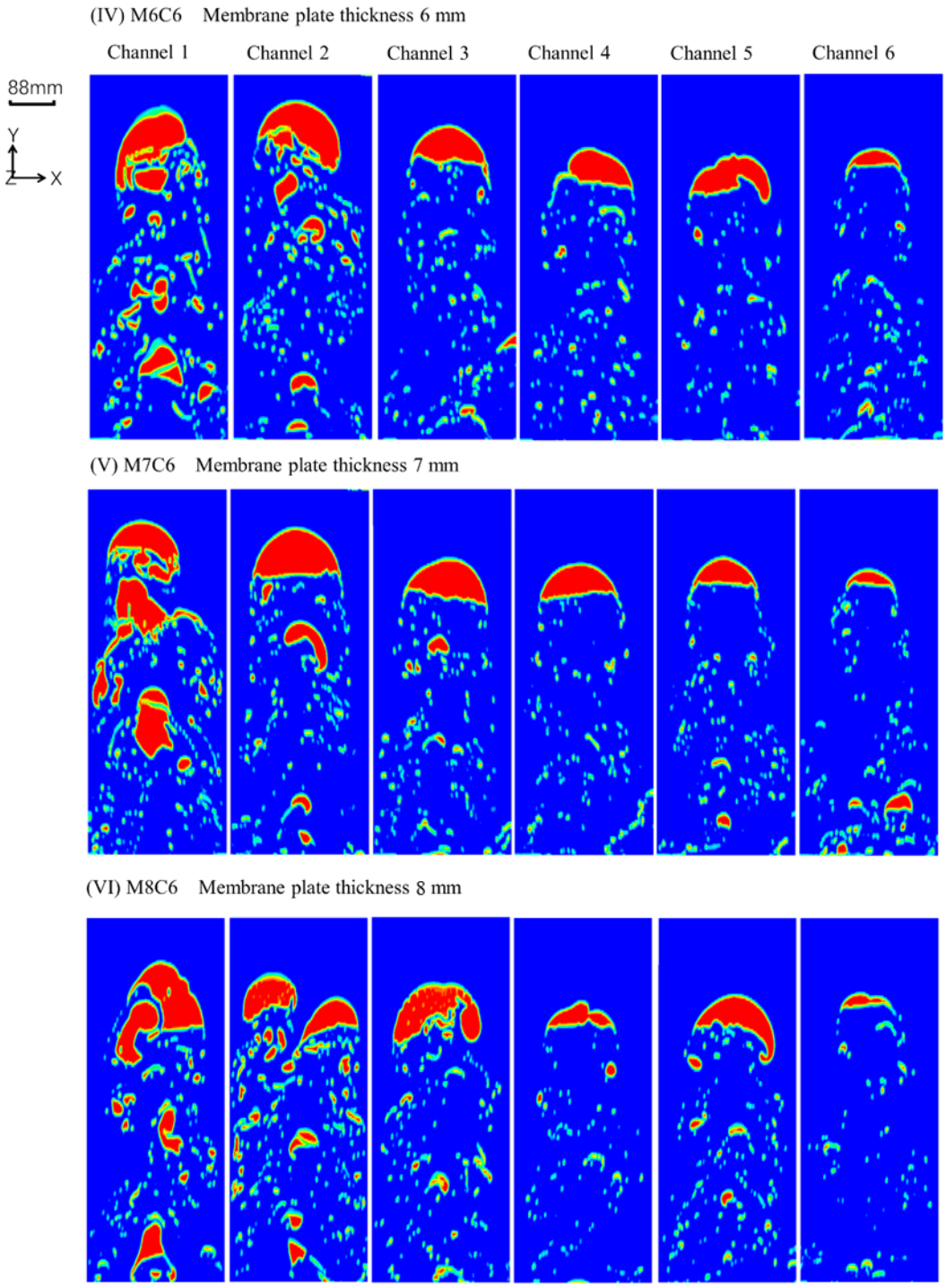

Fig. 11 Bubble distribution comparison for the variation of membrane thickness from 3 mm to 8 mm.

Shear stresses from the slug bubbles in each channel are shown in Fig. 12 (a) and compared for different cases of membrane plate thickness. At cases of M3C6 and M4C6, it could be over 5 Pa for most of the wake regions in the first two channels, while less than 0.5 Pa for the last two channels. As predicted from Fig. 11, compared to the first three channels, the shear in last three channels was dramatically decreased. The shear stress was much stronger in the last few channels for the cases of M5C6, M6C6 and M7C6, due to the larger slug bubbles shown in Fig. 11. For the case of M8C6, although the bubble distribution was less uniform among channels, the membrane surface shear was larger than that of M3C6 and M4C6. Overall the results indicated that the shear stress could be weakened by small membrane plate thicknesses.

From Figs. 9 to 12, it can be seen that the shear stress induced from slug bubbles for the first three channels was always large and over 3.5 Pa, which was independent of the channel or membrane plate thickness. Therefore, more attention should be taken on what happens in the the last few channels since the difference of shear stress on these channels was quite large. Thus the average shear stress is shown in Fig. 12 (b) for all cases. For the first two channels, although the average shear stress was around 5 Pa for the case of M3C6 and M4C6, it has a high value of over 3.5 Pa for all the other cases, indicating that large turbulence induced and the membrane fouling could be effective controlled for these two channels at all membrane thicknesses. The difference of shear stress value increased for the last three channels as the thicknesses of membrane plate varied. It was much lower for the cases of M3C6 and M4C6 (<0.5Pa for the last channel), while it was higher and could be over 1 Pa for all the channels in M5C6 to M8C6. The optimal case would be the one that induced high value of shear stress in all channels including the last few channels. Thus a relative thick membrane plate in the range of 5mm to 8mm should be used in conjunction with our novel bubbling process.

(I) M3C6 Membrane plate thickness 3 mm

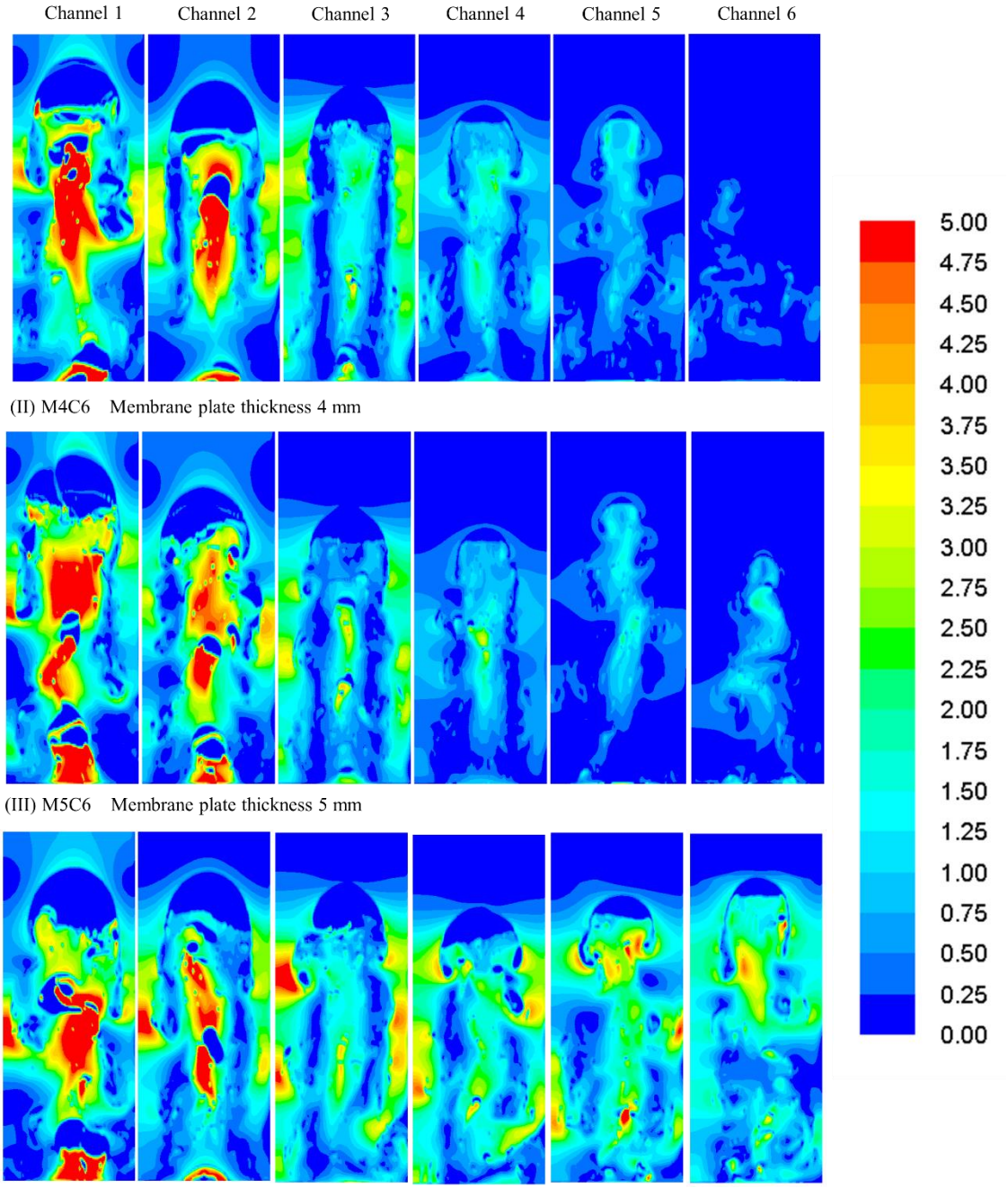

(II) M4C6 Membrane plate thickness 4 mm

(III) M5C6 Membrane plate thickness 5 mm

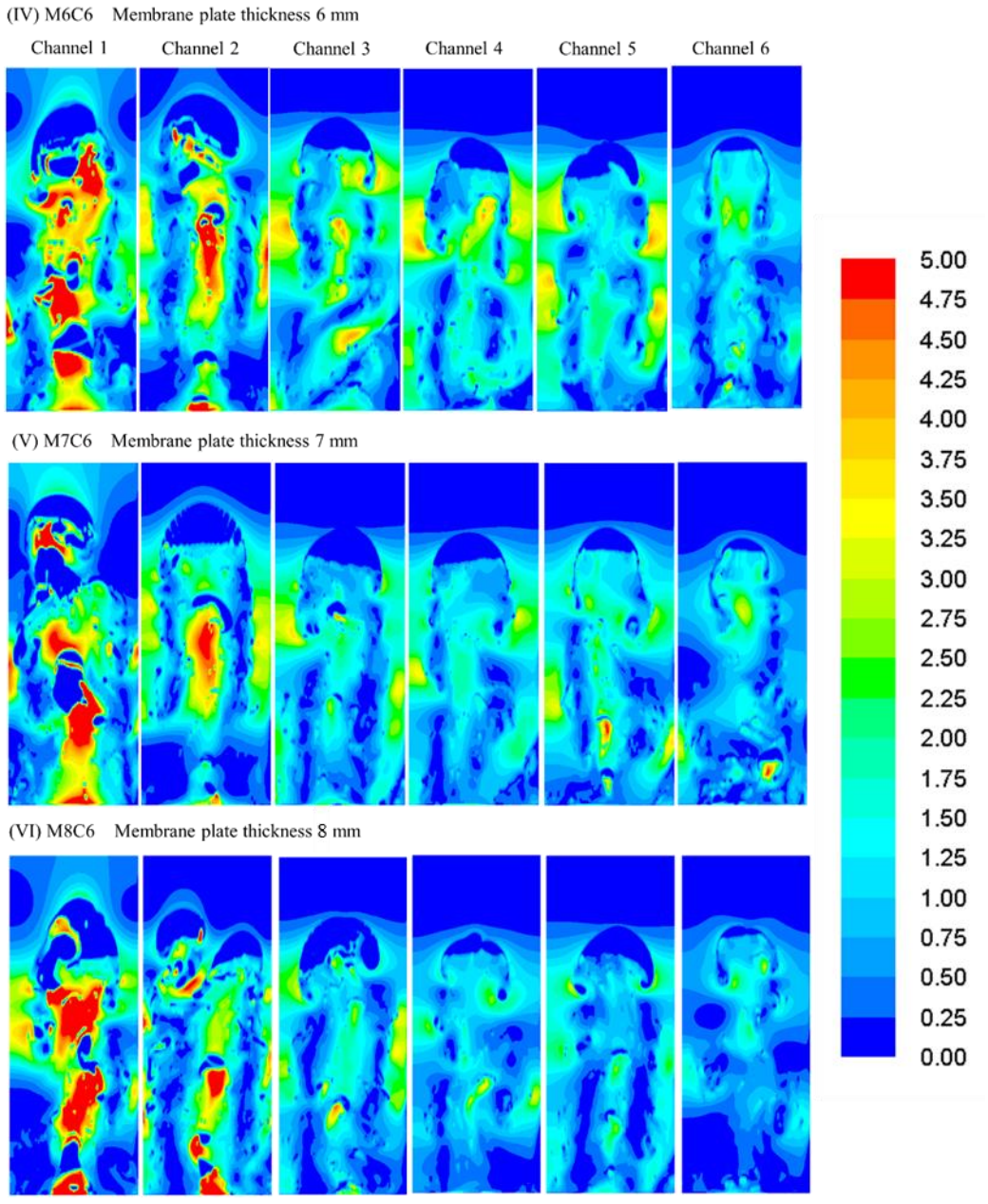
(IV) M6C6 Membrane plate thickness 6 mm
Channel 1
Channel 2
Channel 3
Channel 4
Channel 5
Channel 6
(V) M7C6 Membrane plate thickness 7 mm
(VI) M8C6 Membrane plate thickness 8 mm
5.00
4.75
4.50
4.25
4.00
3.75
3.50
3.25
3.00
2.75
2.50
2.25
2.00
1.75
1.50
1.25
1.00
0.75
0.50
0.25
0.00

(a)

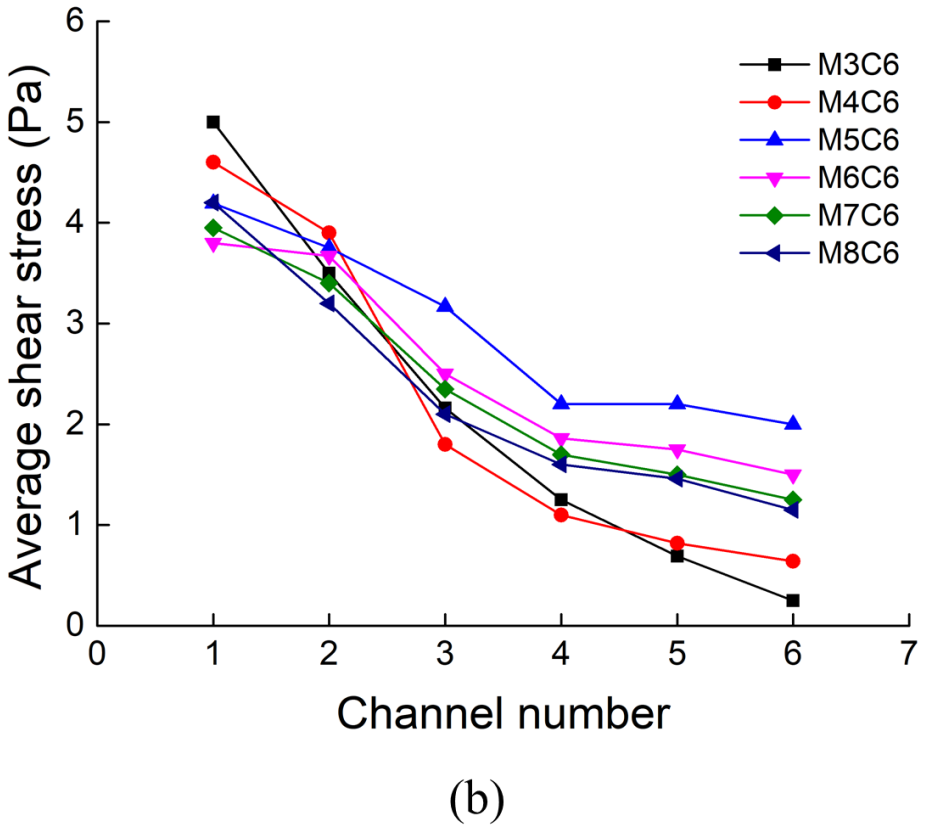

(b)

Fig. 12 Shear stress comparison at different membrane plate thickness from 3 mm to 8 mm: (a) shear stress distribution (b) average wall shear stress.

3.5 Energy Consumption

Based on the above results, the air flow rate per square meter and the total air flow rate for a 100 membrane plates FSMBR have been estimated. By considering the shear stress in Figs. 10 (b) and Fig. 12 (b), the number of channels effectively covered (average shear stress >1.5Pa) from one aerator was calculated for each condition and the results are given in Table 2.

Table 2 Flow rate and energy cost of slug bubbling approach at different conditions

Assumed a FSMBR with 100 membrane plates of 1200mm x510mm x5mm (L xW xT)

Operating Conditions	Channel Gap (mm)	Membrane Plate Thickness (mm)	Number of effective channel coverage	Air flow rate (L/min•m^2)	Total Energy consumption (L/min)	Percentage of energy saved (%)
M5C4	4	5	6	9.5	1206	5
M5C5	5	5	8	7.1	905	29
M5C6	6	5	12	4.7	603	53
M5C6.5	6.5	5	12	4.7	603	53
M5C7	7	5	6	5.7	724	43
M5C8	8	5	6	9.5	1206	5
M3C6	6	3	6	9.5	1206	5
M4C6	6	4	6	9.5	1206	5
M6C6	6	6	12	4.7	603	53
M7C6	6	7	10	5.7	724	43
M8C6	6	8	8	7.1	905	29
Traditional	--	--	--	10	1272	--

A minimum air flow rate of 4.7 L/min·m^2 was found with a channel gap from 5mm to 6.5mm coupled with membrane plate thickness of 5mm and 6mm. The air flow rate was compared with that in industry, and it was found that the savings ranged from 5% to 53%, which indicates that this novel slug bubbling approach could save energy as well as having effective fouling control. The optimal design for this novel bubbling process was considered as M5C6 (membrane plate

thickness of 5mm and channel gap of 6mm) as this produced the most uniform, and high, shear stress distribution.

4. Conclusion

A novel slug bubbling approach has been developed and optimized for a commercial large-scale flat sheet MBRs. This design was investigated and in particular the coalescent bubble size and hydrodynamic features were studied by CFD simulation, and validated experimentally. Shear stress for 6 channels (a symmetric half of a 12 channel system) was compared at different configurations of aerator position and membrane plates. It was found that an aerator below the center membrane producing periodically one large coalescent bubble could provide average shear stresses of more than 2 Pa through all the 12 channels. Based on this configuration, the channel gap (membrane spacing distance) was optimized and found to be between 5mm to 6.5mm. The optimised membrane plate thicknesses were found to be 5mm and 6mm.

In addition to the beneficial hydrodynamic effect that will ameliorate fouling, the simultaneously decrease in the total air flow rate will save up to 53% of the energy compared to the traditional commercial FSMBRs. It is expected that the results of this work will provide the basis for advanced slug bubbling approaches in large-scale FSMBR. It could not only provide an optimization method to set up large-scale FSMBR giving good fouling control, but also reduce the energy usage dramatically so providing an economic advantage. Potentially it may provide a new, practical and economical industrial solution for the treatment of waste water.

Acknowledgements

This work was supported through the grants from the Bureau Frontier Sciences and Education (QYZDB-SSW-DQC044), the Bureau of International Cooperation (132C35KYSB20160018), Chinese Academy of Sciences and Oxiamembrane Co., Ltd, Xiamen, China. We would also like to thank Dr. Olusegun Abass for his help, comments, and assistance.

References

[1] Z. F. Cui, S. Chang, A. Fane, The use of gas bubbling to enhance membrane processes, J. Membrane. Sci. 221 (2003) 1-35.

[2] R. W. Field, K. S. Zhang, Z. F. Cui, B. K. Hwang. Flat sheet MBRs: analysis of TMP rise and surface mass transfer coefficient. Desalin. Water. Treat. 35 (2011) 82-91.

[3] K. S. Zhang, P. Wei, M. Yao, R. W. Field, Z. F. Cui, Effect of the bubbling regimes on the performance and energy cost of flat sheet MBRs. Desalination. 283 (2011) 221-226.

[4] K. S. Zhang, Z.F. Cui, R. W. Field. Effect of bubble size and frequency on mass transfer in flat sheet MBR. J. Membrane. Sci. 332 (2009) 30-37.

[5] O. Iorhemen, R. Hamza, J. Tay. Membrane fouling control in membrane bioreactors (MBRs) using granular materials. Bioresour. Technol. 240 (2017) 9-24.

[6] R. Ghosh, Z.F. Cui, Mass transfer in gas sparged ultrafiltration: upward slug flow in tubular membranes, J. Membrane. Sci. 162 (1999) 91.

[7] Z.F. Cui, Experimental investigation on enhancement of crossflow ultrafiltration with air sparging, in: R. Paterson (Ed.), Effective Membrane Processes-New Perspectives, Mechanical Engineering Publications Ltd, London, 1993, 237–245.

[8] T. Taha, W.L. Cheong, R.W. Field, Z.F. Cui, Gas-sparged ultrafiltration using horizontal and inclined tubular membranes-a CFD study, J. Membrane. Sci. 279 (2006) 487-494.

[9] Q.Y. Li, Z.F. Cui, D.S. Pepper, Effect of bubble size and frequency on the permeate flux of gas sparged ultrafiltration with tubular membranes, Chem. Eng. J. 67 (1997) 71–75.

[10] L. Temmerman, T. Maere, H. Temmink, A. Zwijnenburg, I. Nopens. The effect of fine bubble aeration intensity on membrane bioreactor sludge characteristics and fouling. Water Res. 76 (2015) 99-109.

[11] E. Braak, M. Alliet, S. Schetrite, C. Albasi, Aeration and hydrodynamics in submerged membrane bioreactors, J. Membrane. Sci. 379 (2011) 1-18.

[12] P. Wei, K. Zhang, W. Gao, L. Kong, R.W. Field, CFD modeling of hydrodynamic characteristics of slug bubble flow in a flat sheet membrane bioreactor. J. Membrane. Sci. 445 (2013) 15-24.

[13] H. Prieske, L. Böhm, A. Drews, M. Kraume, Optimised hydrodynamics for membrane bioreactors with immersed flat sheet membrane modules, Desalin. Water. Treat. 18 (2010) 270-276.

[14] X. Liu, Y. Wang, T. Waite, G. Leslie, Numerical simulations of impact of membrane module design variables on aeration patterns in membrane bioreactors. J. Membrane. Sci. 520 (2016) 201-213.

[15] A. Drews, H. Prieske, E.-L. Meyer, G. Senger, M. Kraume, Advantageous and detrimental effects of air sparging in membrane filtration: bubble movement, exerted shear and particle classification. Desaliantion. 250 (2010) 1083-1086.

[16] I. Yamanoi, K. Kageyama, Evaluation of bubble flow properties between flat sheet membranes in membrane bioreactor. J. Membrane. Sci. 360 (2010) 102-108.

[17] P. Culfaza, M. Wessling, R. Lammertink, Fouling behavior of microstructured hollow fiber membranes in submerged and aerated filtrations. Water. Res. 45 (2011) 1865-1871.

[18] L. Xia, L. Wing-Keung, A. Fane, Hydrodynamic effects of air sparging on hollow fiber membranes in a bubble column reactor. Water. Res. 47 (2013) 3762-3772.

[19] M. Pourbozorg, T. Lia, A. Law. Effect of turbulence on fouling control of submerged hollow fibre membrane filtration. Water. Res. 99 (2016) 101-111.

[20] F. Kavousi, E. Syron, M.Semmens, E. Casey, Hydrodynamics and gas transfer performance of confined hollow fibre membrane modules with the aid of computational fluid dynamics. J. Membrane. Sci. 513, (2016) 117-128.

[21] Xie F, Liu J. CFD and experimental studies on the hydrodynamic performance of submerged flat-sheet membrane bioreactor equipped with micro-channel turbulence promoters. Chem. Eng. Process.99 (2016) 72-79.

[22] C. Hirt, B. Nichols, Volume of fluid (VOF) method for the dynamics of free boundaries. J. Comput. Phys. 39 (1981) 201-225.

[23] T. Shih, W. Liou, A. Shabbir, Z. Yang, J. Zhu, A new Kappa-Epsilon eddy viscosity model for high Reynolds-number turbulent flows. Comput. Fluids. 24 (1995) 227-238.

[24] W. Reynolds, Fundamentals of turbulence for turbulence modeling and simulation. Lecture Notes for Von Karman Institute, Agard Report. No. 755. (1987).

[25] FLUENT 17.0 Theory Guide (2017), ANSYS, Inc., Pennsylvania.

[26] J. Brackbill, D. Kothe, C. Zemach, A continuum method for modeling surface-tension. J. Comput. Phys. 100 (1992) 335-354.